Modeling optical properties of mineral dust over the Indian Desert

S. K. Mishra[1] and S. N. Tripathi[1]

[1]   The direct radiative forcing (DRF) of dust particles is most uncertain among all the major aerosol species because of the large regional variation in their shapes and composition. The Indian Desert is known to be a source of natural mineral dust of nonspherical shapes. Particle shape and exact mineralogical information are essential for modeling dust optical properties as the latter governs their refractive indices. The realistic dust shapes, namely, sphere, spheroid, Chebyshev, and cylinder, based on Scanning Electron Microscope (SEM) images, have been used to model the mineral dust optics of the Indian Desert using the T-matrix method. The particle radius from 0.1 to 5.0 μm has been considered at wavelengths ranging from ultraviolet to near infrared (0.38–1.2 μm). Using Bruggman's effective medium mixing rule, the refractive index of composite dust particle has been calculated, accounting for both nonmetallic and metallic component (as hematite). Our calculations show that increasing the hematite percentage from 0% to 10% results in reduction of 0.477 and 0.013 in single scattering albedo (SSA) for cylindrical particle of radius 1 μm at 0.38 and 1.02 μm wavelengths, respectively, while the same for volume equivalent spherical particle were 0.484 and 0.022, respectively. The scattering signature of sharp-edged cylindrical particle showed the largest deviation to sphere compared with that of other relatively smooth particles (spheroid and Chebyshev). Changes in dust optical properties because of nonsphericity and varying hematite percentage were estimated for two cases: background dust and dust storm at visible wavelength. The change in SSA between the above two cases was insignificant for particles of radii <0.4 μm for each hematite percentage considered. On the other hand, for particles of size range 0.4–1 μm, the change in SSA increases with increasing hematite percentage. A 6% increase in hematite leads to an SSA reduction of more than 0.2 for particle radius of 1 μm for both background dust and dust storm cases. Optical properties of polydisperse dust distribution at visible wavelength suggest the likely hematite percentage as 0%–4% in the Indian mineral desert dust. The effect of hematite variation on SSA is found to be stronger than particle nonsphericity. The present work will lead to a better estimation of the radiative forcing imposed by dusts as well as their satellite retrieval over the Indian Desert region.

1. Introduction

[2]   The direct radiative forcing (DRF) imposed by aerosol is uncertain to large extent, and rely on the estimations from observational and global modeling studies [*Forster et al.*, 2007]. The top-of-atmosphere (TOA) DRF of the composite aerosol as a global annual mean quantity inclusive of the effects of clouds has been reported to be -0.50 ± 0.40 Wm^{-2} [*Forster et al.*, 2007]. However, among all the individual major aerosol components (sulfate, black carbon, sea salt and dust) dust by far is most uncertain with net TOA dust radiative effect reported to be as -0.56 to $+0.1$ Wm^{-2} [*Forster et al.*, 2007].

[3]   Dust particles interact with a wide spectrum of radiation (UV to infrared) making its radiative effects quite complex than various other types of atmospheric aerosols. The forcing imposed by the mineral dust may lead to the heating or cooling of the climate system [*Haywood and Boucher*, 2000]. Modeling estimates of dust radiative forcing [*Ginoux et al.*, 2001; *Weaver et al.*, 2002; *Myhre et al.*, 2003; *Collins et al.*, 2001; *Miller and Tegen*, 1998] together with ground based, aircraft and satellite observations [*Tanré et al.*, 2003; *Highwood et al.*, 2003; *Hsu et al.*, 2000; *Haywood et al.*, 2003a, 2003b; *Kaufman et al.*, 2001] emphasize the complexity of dust-radiation interaction. *Sokolik and Toon* [1996], using a box model, calculated the global-mean direct solar radiative forcing of mineral

[1]Department of Civil Engineering, Indian Institute of Technology Kanpur, Kanpur, India.

aerosol due to anthropogenic activity such as inappropriate irrigation practices, excessive cultivation of poor soils, heavy grazing, urbanization and human induced wind erosion. The calculated global-mean direct solar radiative forcing are -0.25 Wm^{-2} over land and -0.6 Wm^{-2} over ocean with an uncertainty range of -0.08 to -0.9 and -0.2 to -2.2 Wm^{-2}, respectively. The Earth Radiation Budget Experiment (ERBE) observations have revealed that the radiative forcing imposed by mineral dust near the dust source is comparable to those of clouds [*Harrison et al.*, 1990].

[4] The dust load in the atmosphere alters the surface radiation budget leading to change in surface temperature and thus the surface-air exchange process get perturbed thereby influencing the atmospheric dynamics. So, proper estimation of radiative impact of mineral dust is important because of their wide spatial coverage and large optical depth. Numerical simulation study of the spatial distribution of dust by *Tanaka and Chiba* [2006] shows that the greatest contributor to the global dust budget is the Sahara Desert while dust load from East Asia (Eastern and Western China) is not ignorable. In this study, dust from East Asia dominates over China, Mongolia, Korea, Japan, and the North Pacific Ocean whereas Australian dust was found to be dominating in the southern hemisphere. Mineral dust has been found to be the biggest contributor to aerosol optical thickness in various arid regions of the world [*Tegen et al.*, 1997; *Houghton et al.*, 2001].

[5] Dust particle optics is region specific [*Kubilay et al.*, 2003; *Dubovik et al.*, 2002]. The limited knowledge of the optical properties of the regional dust aerosol is a major constraint to the accurate net radiative forcing estimates (both magnitude and sign). The sign and magnitude of the radiative forcing, imposed by mineral dust, is governed by its optical properties such as single scattering albedo (w_0), asymmetry parameter and extinction coefficient [*Liao and Seinfeld*, 1998], which remain uncertain because of limited information on dust morphology and mineralogy which have large spatiotemporal variation [*Sokolik et al.*, 2001]. A more adequate assessment of the regional radiative forcing imposed by mineral dust could be made only after the morphological and mineralogical information of the regional dust become available.

[6] The dust aerosol is a composite mixture of different minerals as shown by *Reid et al.* [2003a, 2003b]. Proportions of the mineral components and their mixing solely rely on dust source and physicochemical transformations during transportation of the dust in the atmosphere. The contributing mineral components show wide range of optical parameters. The effective refractive indices of the composite mineral dust are estimated based on the mineral composition proportions, their mixing state and optical parameters of individual mineral component. Thus, to study the optical properties of the mineral dust, the proportion of each mineral component together with their mixing state is required. The sensitivity study by *Myhre and Stordal* [2001] also emphasized the importance of chemical composition and hence the refractive index of individual component to the forcing imposed by mineral dust.

[7] Earlier, dust optics has been studied by numerical simulations and laboratory experiments. *Mishchenko et al.* [1997] reproduced the optical signatures of the mineral dust by considering the dust to be mixture of randomly oriented spheroids of different aspect ratios and sizes. Later, *Dubovik et al.* [2002, 2006] considered dust as mixture of randomly oriented spheroids to retrieve aerosol optical properties from AERONET ground-based radiometers while *Kalashnikova and Sokolik* [2002, 2004] considered various complicated shapes based on Scanning Electron Microscope (SEM) images for modeling the desert dust optics. The modeling studies have also been linked with the experiments by *Nousiainen and Vermeulen* [2003] who compared experimental and modeled results for feldspar particles. *Yang et al.* [2007], based on their modeling study, concluded that the effect of dust particle nonsphericity is negligible in thermal infrared wavelengths while it plays a significant role in short wavelengths.

[8] In Indian subcontinent, the dust storms are prominent in northern and north-western parts of India in pre-monsoon (March–May) season when south westerly wind transport mineral dust from the Thar desert, also described as 'The Great Indian Desert', lying in the north-west part of India, and spanning over an area of 0.32×10^6 km^2 [*Sikka*, 1977]. The developing surface low pressure in North–West of India in this season [*Singh et al.*, 2005] lifts the mineral dust to high altitude together with significant spatial spreading. Several studies [*Dey et al.*, 2004; *Chinnam et al.*, 2006] have investigated how dust, brought by the dust storms from the Thar desert, mix with the anthropogenic pollution and affect the optical properties of aerosols over Indo-Gangetic basin. It is therefore important to quantify the optical properties of the pure dust to understand the effects of the mixing of natural and anthropogenic components in this region. To the best of our knowledge the only study that modeled dust optical properties over the Indian Desert was by *Peterson and Weinman* [1969]. They computed the optical properties considering dust particles to be spherical and composed purely of quartz.

[9] No earlier study has been done till date for calculating optical properties of the mineral dust over the Indian Desert with realistic dust composition and particle shapes based on previous experimental results. *Moorthy et al.* [2007] inferred single scattering albedo, SSA, at visible wavelength to be $0.88–0.94$ of dust over the Indian Desert using ground based multiwavelength solar radiometer (MWR) and first generation meteorological satellite, METEOSAT-5 using the method proposed by *Deepshikha et al.* [2005] (for more details readers may refer to *Deepshikha et al.* [2005]).

[10] In the present study, optical properties of the mineral dust originating from the Thar desert have been modeled. These mineral dust particles are mostly nonspherical, sharp edged in shape, which exhibit different scattering signature compared to that of volume equivalent spheres while interacting with the incident radiation [*West et al.*, 1997; *Volten et al.*, 2001]. Sampling over Gurushikar, Mt. Abu (Rajasthan) has revealed elemental concentration of atmospheric dust and particle shape information from SEM analysis of sampled dust [*Negi et al.*, 1996, 2002]. Unfortunately, the study of *Negi et al.* [1996, 2002] did not provide the mineralogical composition of the sampled dust particles. The earlier mineralogical analysis of desert dust revealed only the nonmetallic composition [*Peterson*, 1968] whereas the subsequent studies [*Negi et al.*, 1996, 2002] indicated that the contribution of metallic mineral (e.g., iron) cannot be ignored while constructing the mineralog-
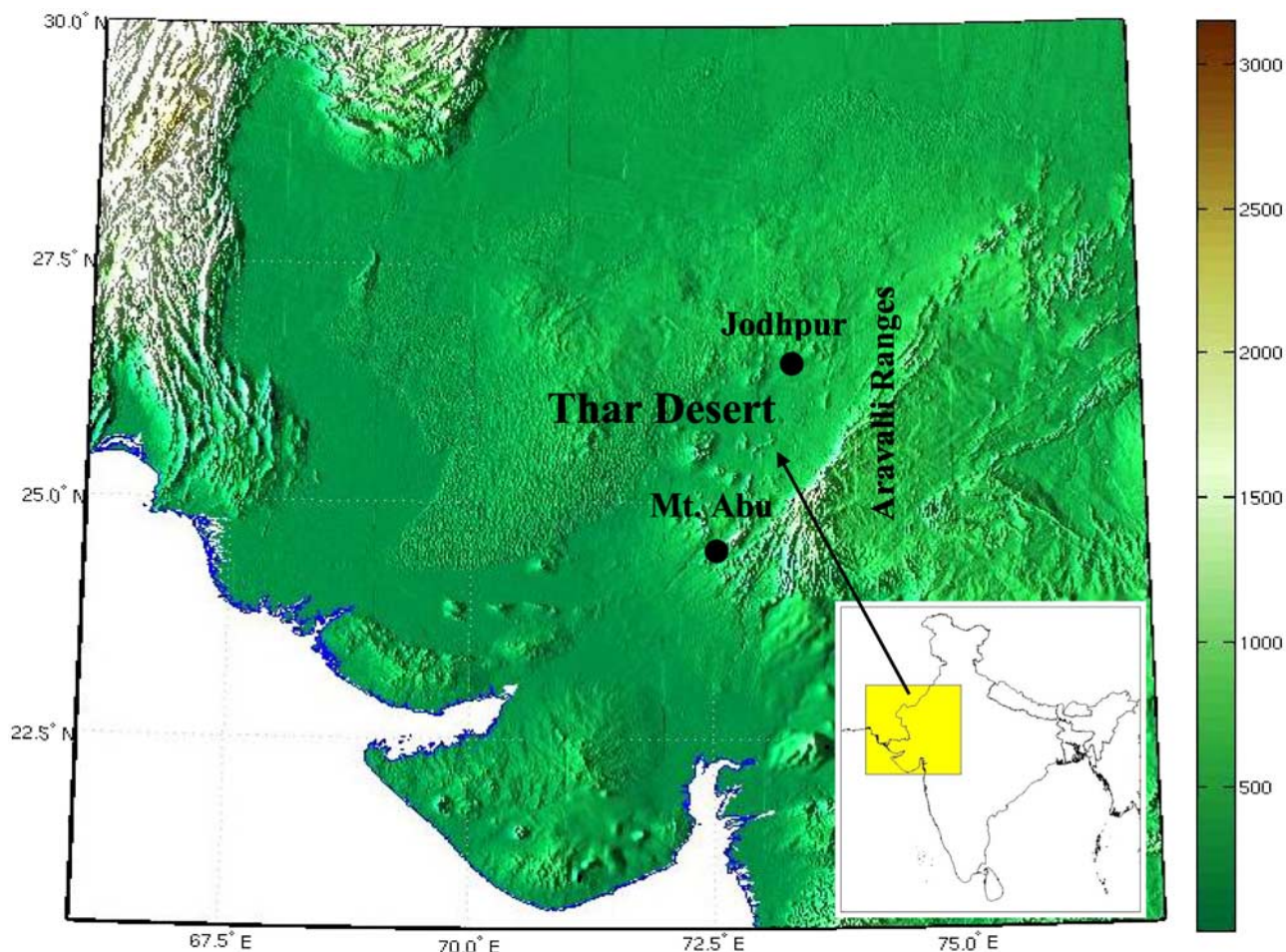
Figure 1. Schematic of the study region (the column in right is showing the altitude in meter).

ical composition of Rajasthan dust. The iron present in the atmospheric dust oxidizes to form Hematite (Fe_2O_3), which is a good absorber of radiation in the ultraviolet and visible wavelength range [*Sokolik and Toon*, 1999; *Lafon et al.*, 2006]. The present study uses the shape and mineralogical information from *Negi et al.* [1996, 2002] and *Peterson* [1968].

2. Study Region

[11] The Indian Desert is an extensive arid region with dimensions 800 km long and 400 km wide in north–west of India and east of Pakistan lying between the Indus and Sutlej river valleys on the west and the Aravalli Range on the east (Figure 1). This desert is a large desolate region of shifting sand dunes, broken rocks, and scrub vegetation with the annual average rainfall of less than 25 cm. The probability of severe drought period is four out of ten years during which strong winds prevail blowing for nearly half of the year in this region. The more humid conditions that prevail near the Aravallis prevent the extension of Thar Desert toward the east and the Ganges Valley.

3. Dust Morphology and Index of Refraction

[12] The air sampling from January–March 1994 for dust collection was conducted at an altitude of 14 m from the ground at Mt. Abu (asl of 1219 m.), Rajasthan [*Negi et al.*, 1996]. Glass fiber filters were used to collect total suspended particulate matter (TSPM) whereas Whatman 541 filters were used for elemental composition of dust. Total 20 samples were collected; 10 on glass fiber filter and Whatman 541 filter each using the high-volume sampler. The dust load over the site was found to be 80–100 μgm^{-3} during clear days, 200–500 μgm^{-3} during dusty days (from May–June) while it was found to be reduced to 20–60 μgm^{-3} in October [*Meenakshy and Sadasivan*, 1993]. Size and shape analysis was done after spreading the dust evenly on clean aluminum foils. Kevex Scanning Electron Microscope (SEM) equipped with electron excited X-ray Fluorescence (XRF) analysis was used to determine the shape, size and elemental composition of the dust particles. Figure 2 shows the SEM photograph of sampled dust particles, indicating the nonspherical shape of the dust particles collected at Mt. Abu.

[13] On the basis of the SEM images, model shapes were assumed that are closest to the various shapes observed in the image. In the present study, the modeled dust particle shapes are sphere, spheroid, cylinder and Chebyshev. The aspect ratio (ratio of the particle's length to its width) based on the statistical representative data on dust morphological properties collected after sampling of several thousands of dust particles in the atmosphere was found to be 1.5
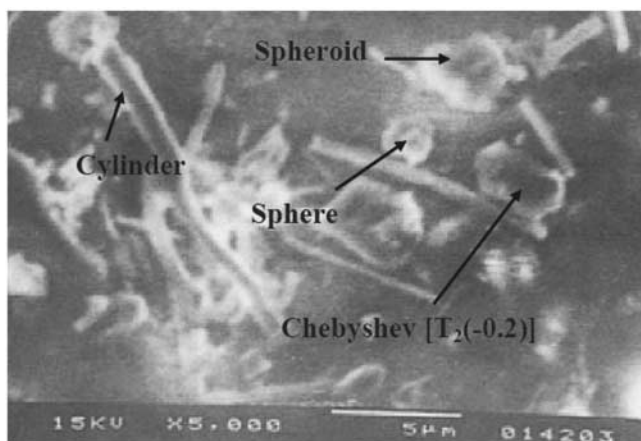
Figure 2. Scanning Electron Microscope (SEM) image of dust particles collected at Gurushikar, Mt. Abu. Adapted from *Negi et al.* [1996].

[*Parungo et al.*, 1997]. The shape of atmospheric mineral particles of radius $0.1-6$ μm, sampled in three arid regions of China, showed the median aspect ratio to be 1.4 after electron microscopic study [*Okada et al.*, 2001]. However, the aspect ratio of 1.5 is a more representative value for mineral dust as suggested by *Parungo et al.* [1997] and *Anderson et al.* [1992]. The small nonspherical particle (<1 μm), with aspect ratio 1, shows nearly same scattering signature as that of volume equivalent sphere whereas the increase in aspect ratio (>1) enhances the difference in the scattering signature to its equivalent sphere [*Asano and Yamamoto*, 1975]. Among the naturally existing dust particles, the so-called Chebyshev particles are rotationally symmetric particles, a shape obtained after continuous deformation of a sphere by means of Chebyshev polynomial of degree n. The shape of the particles in the natural coordinate system is given as [*Mishchenko and Travis*, 1998]:

$$r(\theta, \phi) = r_0[1 + \varepsilon T_n(\cos\theta)], \qquad |\varepsilon| < 1 \qquad (1)$$

where r_0 is the radius of the unperturbed sphere, ε is the deformation parameter whose value leads to the different shapes of Chebyshev particles formed after deforming the sphere. T_n is the Chebyshev polynomial of the first kind of degree n with the trigonometric definition $T_n(\cos\theta) = \cos n\theta$.

[14] The recurrence relation for above polynomial is:

$$\begin{aligned} T_0(x) &= 1 \\ T_1(x) &= x \\ T_{n+1}(x) &= 2x\,T_n(x) - T_{n-1}(x) \end{aligned} \qquad (2)$$

Surface roughness of the particle appears in the form of waves running around the particle and the numbers of waves increase linearly with the parameter n. The modeled Chebyshev particle with order, $n = 2$, and the deformation parameter, $\varepsilon = -0.2$, is expressed as $T_2(-0.2)$. We consider the above particle because of its close resemblance to some

images shown in Figure 2. However, the presence of other Chebyshev particles in the dust with different order and deformation parameter cannot be ignored. So we included other Chebyshev particles viz. $T_2(0.2)$, $T_4(-0.15)$ and $T_6(0.1)$ as well in our computations. Hereafter we will refer Chebyshev particles $T_2(-0.2)$, $T_2(0.2)$, $T_4(-0.15)$ and $T_6(0.1)$ as chby1, chby2, chby3 and chby4, respectively. The model shapes to compute the particle optics are given in Figure 3.

[15] The studies by *Negi et al.* [1996, 2002] have also revealed the size of dust particles from the SEM analysis indicating presence of small (particle diameter, $D_p \leq 5$ μm) and large particles ($D_p \geq 50$ μm) (defined by *Negi et al.* [1996, 2002]). Particles with size $1-5$ μm were found embedded on the surface of the large particles. Unfortunately, the relative abundance of the small and large particles to the mineral dust load was not investigated in the above study. It has been shown earlier that the smaller particles (particle diameter ≤ 5 μm), because of their high residence time, interact more with the incoming radiation compared to large particles. Although the presence of larger particles near the source cannot be ignored, their contribution to the total global annual averaged dust load is negligible [*Miller et al.*, 2006]. The modeling study by *Miller et al.* [2006] revealed that the total global annual averaged dust load in the atmosphere is mainly due to dust particles of radii <10 μm with those of radii $1-2$ μm making the largest contribution to it. Thus, in the present study, for modeling the optical properties of the dust in the atmosphere, we considered the particle radii from $0.1-5$ μm, which covers major range of atmospheric dust size, at least, from the optics point of view.

[16] In order to determine the index of refraction of dust particles, which is an input parameter in optical calculations, it becomes imperative to fix the mineralogical composition of dust. The only mineralogical analysis revealing the relative constituent abundance available, to the best of our knowledge, was by *Peterson* [1968]. Over north–west India (Rajasthan), *Peterson* [1968] found that the relative abundance of basic nonmetallic minerals such as Quartz, Feld-
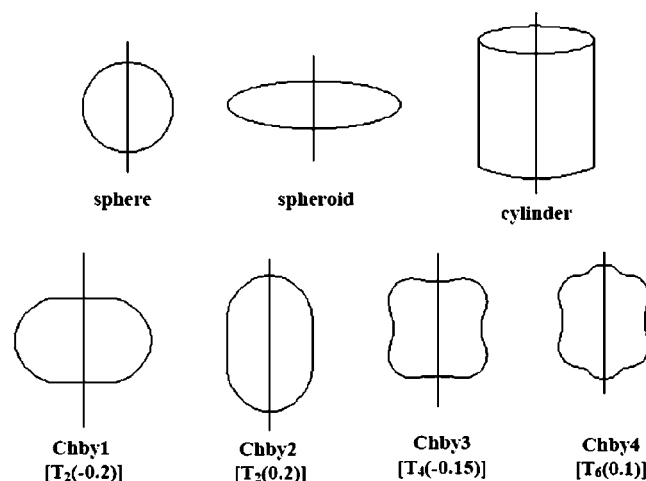

Figure 3. Model shapes with their axis of symmetry, assumed on the basis of SEM image of dust particles collected at Gurushikar, Mt. Abu.

Table 1. Optical Parameters of Mineral Dust Components Over the Indian Desert[a]

Mineral Component	Wavelength (μm)	Reference
Quartz		
Crystalline	$1.5*10^{-5}$ to $3.3*10^{2}$	*Palik* [1985]
Crystalline	0.768 to 36	*Peterson and Weinman* [1969]
Feldspar	0.185 to 2.6	*Egan and Hilgeman* [1979]
Mica	0.185 to 2.6	*Egan and Hilgeman* [1979]
Calcite		
Amorphous	2 to 32.8	*Querry et al.* [1978]
Crystalline	2.5 to 300	*Long et al.* [1993]
Crystalline	0.2 to 6	*Ivlev and Popova* [1973]
Hematite	0.2 to 50	*Querry et al.* [1978]
	8.3 to 50	*Popova et al.* [1973]

[a]The last column shows the source from where these values were taken.

spar, Mica and Calcite in dust particle as 36%, 22%, 20% and 20%, respectively. The above mineral components possess negligible imaginary part of refractive index at wavelengths $0.38–1.2$ μm. However, earlier studies [*Sokolik and Toon*, 1999; *Lafon et al.*, 2006; *Koven and Fung*, 2006] revealed the existence of iron in the form of hematite (Fe_2O_3) in dust. *Sokolik and Toon* [1999] emphasized the importance of hematite as a major component in the dust controlling light absorption at solar wavelengths. The study by *Bishop et al.* [2002] also revealed the dust as the key source of iron to remote ocean water. On the basis of AERONET-retrieved refractive indices, *Koven and Fung* [2006] inferred the hematite fraction to be $3.75–11.97\%$ in global dusts. For Indian dust, no exact volumetric percentage of hematite is known till date, so we have included hematite in the dust and performed sensitivity study of the Fe content. The study by *Negi et al.* [1996, 2002] and exploration made by Department of Mines & Geology, Government of Rajasthan (http://www.dmg-raj.com/mineral_reserves.html) detected the occurrence of metallic mineral, Fe, in the desert dust.

[17] The effective refractive index of the nonmetallic mineral constituents has been calculated using volume weighted average, whereas effective refractive index of composite mineral dust (nonmetallic + metallic) has been calculated using Bruggman's effective medium mixing rule [*Bohren and Huffman*, 1998]. On the basis of the study of *Peterson* [1968], effective refractive index of nonmetallic part of dust (A) has been calculated using summation of individual index of refractions with their weights of volume or mass fractions as:

$$m_{eff}^{A} = \sum f_i m_i \qquad (3)$$

Where m_{eff}^{A} is the effective index of refraction of the part A of mineral dust, m_i is the refractive index of ith mineral component with f_i volume (or mass) fraction. The contribution of Fe to mineral dust in form of its oxide (Fe_2O_3) will be hereafter referred to as metallic composition, B, in the present study. The variation of Fe_2O_3 has been constrained within the range $0–10\%$ based on the previous experimental observations [*Choi et al.*, 2001; *Lafon et al.*, 2001] with a global mean of 6.85% [*Goudie*, 1978].

[18] The effective refractive index of the mineral dust with its constituents as A and B then has been found using Bruggman's effective medium mixing rule [*Bohren and Huffman*, 1998, 217 pp.] as:

$$f\frac{\varepsilon_A - \varepsilon_{eff}}{\varepsilon_A + 2\varepsilon_{eff}} + (1 - f)\frac{\varepsilon_B - \varepsilon_{eff}}{\varepsilon_B + 2\varepsilon_{eff}} = 0 \qquad (4)$$

Where ε_A and ε_B are the complex dielectric constants of the constituents A and B, respectively, and f is the volume fraction of A. ε_{eff} is the effective complex dielectric constant of the composite dust particle. In this expression real (ε_r) and imaginary (ε_i) part of complex dielectric constants (ε) of A and B have been calculated as:

$$\varepsilon_r = n^2 - k^2$$
$$\varepsilon_i = 2nk \qquad (5)$$

Where n and k are real and imaginary part of refractive index (m), $m = n + i\,k$. Values of n and k for the constituents of A and B have been taken from literature as given in Table 1. Effective refractive index for 0% hematite case, i.e., dust containing only nonmetallic minerals (A), has been calculated using equation (3), with the optical parameters at the selected wavelengths (Table 1) and the fractional percentage of constituents of A given by *Peterson* [1968]. Thus obtained effective refractive index ($m_{eff} = n_{eff} + i\,k_{eff}$) was used to calculate the real and imaginary part of complex dielectric constants at each wavelength using equation (5).

[19] For metallic component, B, the complex dielectric constants was evaluated using optical parameters from Table 1 and equation (5). Then the effective dielectric constant of the composite mineral was found using equation (4). The effective dielectric constants are evaluated by varying the hematite volume percentage from $0–10\%$. The calculated effective dielectric constants with their real and imaginary parts are used to solve the equation (5) for effective optical parameters of composite mineral dust. Spectral variation of real and imaginary indices of composite mineral dust for varying fraction of B is shown in Figure 4.

[20] Optical characteristics of dust aerosols are very sensitive to its optical parameters. In absence of B, n has highest value at the lowest wavelength (0.38 μm) which decreases with increasing wavelength. On the other hand k shows larger values at largest wavelength (1.2 μm) besides at the lowest wavelength. With increasing hematite fraction, values of n and k were found to be increasing which is prominent at ultraviolet and visible wavelengths. In the infrared region (>0.7 μm), in general the spectral variation shows a decreasing trend of n and k for different hematite fraction. The overall trend in spectral variation of n and k, in Figure 4, resembles to those of clay component with varying hematite volume percentage studied by *Lafon et al.* [2006]. *Carlson and Caverly* [1977] also reported the similar spectral variation of k for the Saharan dust.

4. Model Details

[21] Optical properties of the mineral desert dust have been computed using T-matrix code [*Mishchenko and Travis*, 1998] which is publicly available on the World
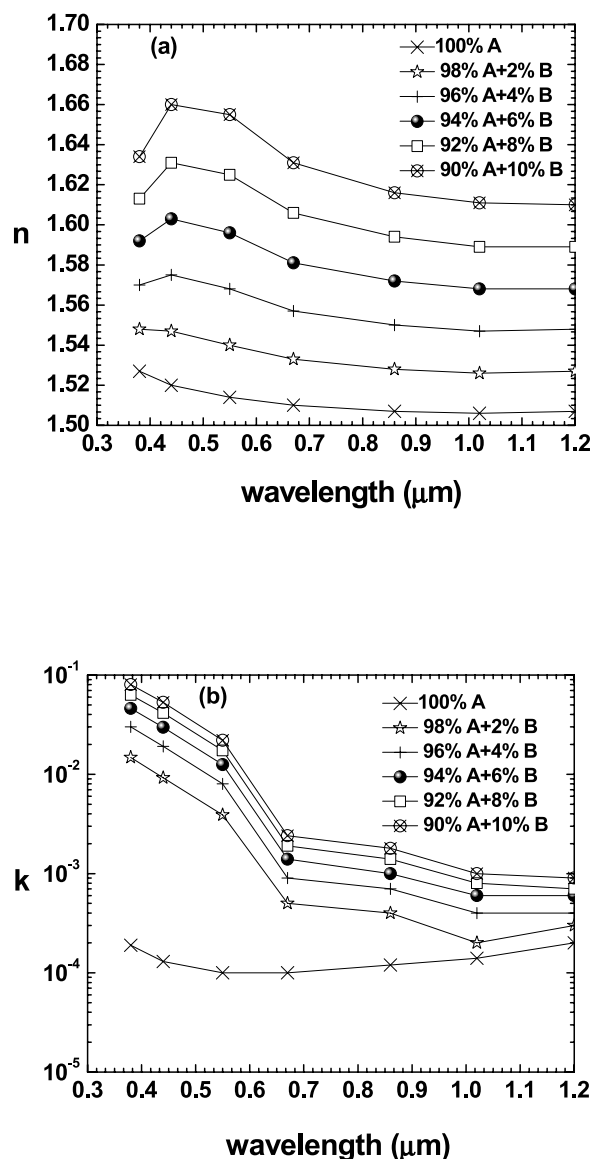
Figure 4. Spectral variation of (a) real (n) and (b) imaginary refractive index (k) of composite mineral dust over the Indian Desert with varying fraction of B (hematite).

Wide Web at http://www.giss.nasa.gov/~crmim. T-matrix method computes light scattering for polydisperse, randomly oriented, rotationally symmetric particles such as sphere, spheroid, cylinder and Chebyshev particles. The volume equivalent radius of the nonspherical particle (r_{eff}), refractive index, wavelength (μm), particle shape and the aspect ratio are the inputs to the T-matrix code. The outputs of the code are extinction and scattering cross-sections (C_{ext} and C_{sca}), asymmetry parameter (g), SSA and scattering matrix elements. The T-matrix code has been tested and verified with the results earlier published by *Kalashnikova and Sokolik* [2004] for exactly similar conditions.

[22] As there is no difference in the computed optical properties from T-matrix code and Mie code [*Dave*, 1968] for spheres therefore for the calculation of optical properties of spherical particle we have used Mie code. Moreover, Mie

code is less CPU time consuming compared to T-matrix code for large size spherical particle. Using this code, the optical properties have been computed for a given size, wavelength and refractive index. The algorithm in the program solves Helmholtz equation in the spherical coordinate system. Optical properties such as extinction, absorption and scattering efficiencies of the spherical particle for a given size parameter and index of refraction are computed using the code.

5. Results and Discussion

[23] The optical properties of mono-disperse, nonspherical and pure mineral dust particles are computed although the dust particles in the atmosphere are polydisperse in nature. For most of the present calculations, the particles have been considered as mono-disperse for two reasons: (1) to study the effect of nonsphericity only on the particle optical properties, and (2) because the exact distribution parameters are not known. However, some polydisperse calculations have also been done for the log-normally distributed dust. The log normal distribution with median radius, r = 0.5 μm and a geometric standard deviation, σ = 1.5 has been considered as a typical dust representative distribution based on earlier research [*Dubovik et al.*, 2000; *Reid et al.*, 2003a, 2003b].

[24] In the present study, optical properties such as SSA, C_{ext}, C_{sca} and g of the dust particles have been studied for a given size range (0.1–5 μm) and composition. As the refractive index is a strong function of wavelength [*Sokolik and Toon*, 1999], a wavelength range has been chosen to study mineral dust particle optics. The selected wavelength range from 0.38 μm–1.2 μm covers entire shortwave region, which is important for understanding shortwave radiative impacts.

[25] Variation of dust particle optics has been shown with particle size parameter, α, defined as the ratio of perimeter of the particle to the interacting wavelength. Figure 5 shows SSA of dust particle varying with particle size and size parameter, α (top x axis), and the same has been shown in the inset for the particles with radius <1 μm for better visualization. The volume fraction of hematite has been considered to be zero in this case. SSA was found to be varying from 0.97–1 in the considered wavelength domain for a given size range for particles of different shapes. In Figure 5a, beyond size parameter 30, T-matrix could converge only for chby1, chby2 and spheroid particles. Increasing particle size leads to slight reduction in SSA. In the inset, at 0.38 μm the SSA of nonspherical particles is equal to that of volume equivalent spheres for $\alpha \leq 3$ while it deviates for the greater values of α but not in a regular way. In Figures 5b, 5c and 5d, the reduction in SSA with size decreases with increasing wavelength. In the insets of above figures, for visible range, for $\alpha \leq 4$–4.8, the nonspherical particles show negligible difference to that of equivalent sphere while beyond that latter show less SSA values. Among the nonspherical particles, sharp-edged cylindrical particles show largest deviation from spherical one compared to that of smooth nonspherical particles such as Chebyshev and spheroids. Figures 5e, 5f and 5g depict the SSA reduction with the increasing size. From the insets of above figures, at the near infrared regime, it can be seen
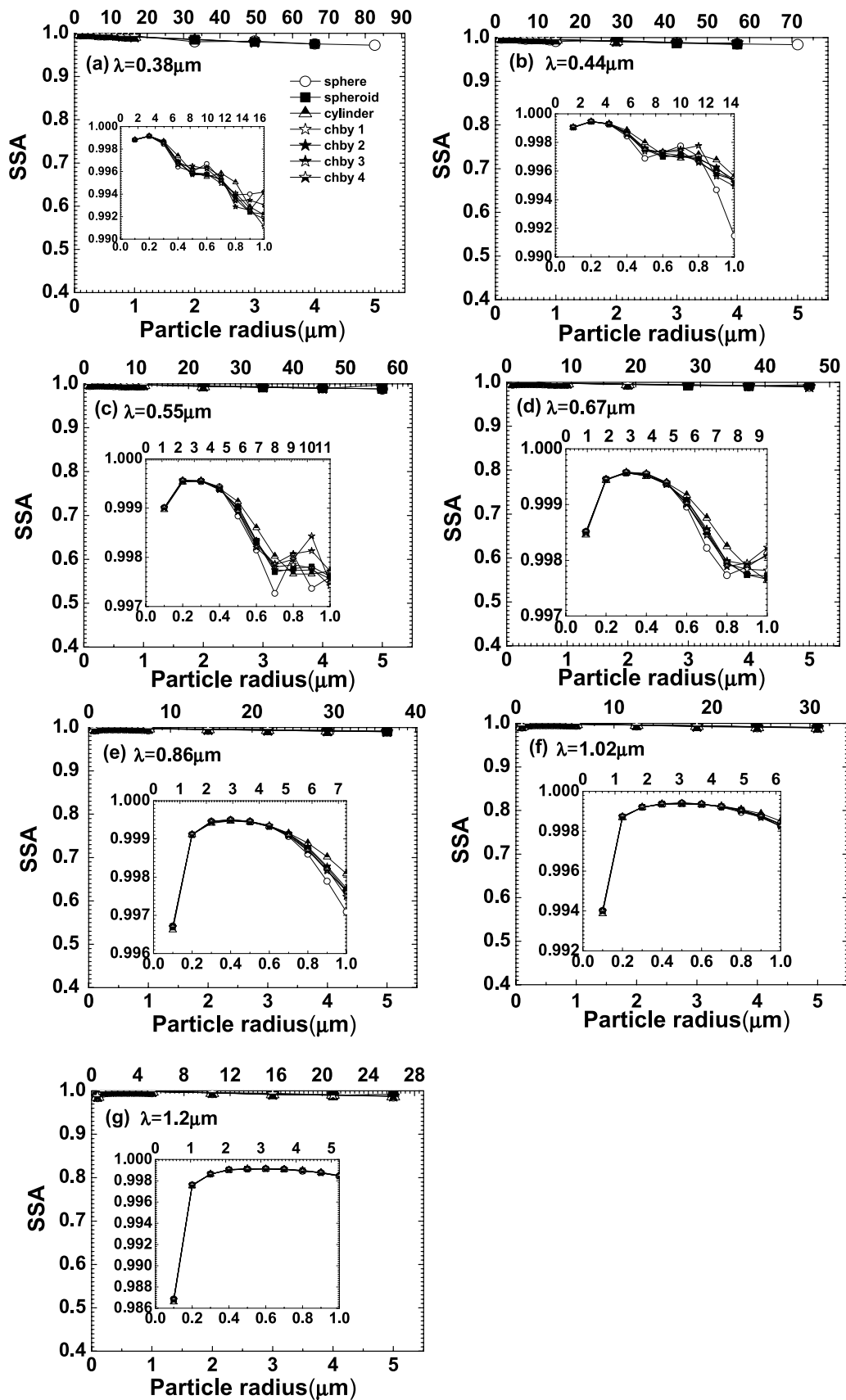
Figure 5. Single Scattering Albedo (SSA) variation of dust for 0% hematite as a function of particle radius at wavelength (a) 0.38, (b) 0.44, (c) 0.55, (d) 0.67, (e) 0.86, (f) 1.02, and (g) 1.2 μm. The top x axis in each plot represents the size parameter α. The inset in the subfigures shows the same variation but for particle radius <1 μm.
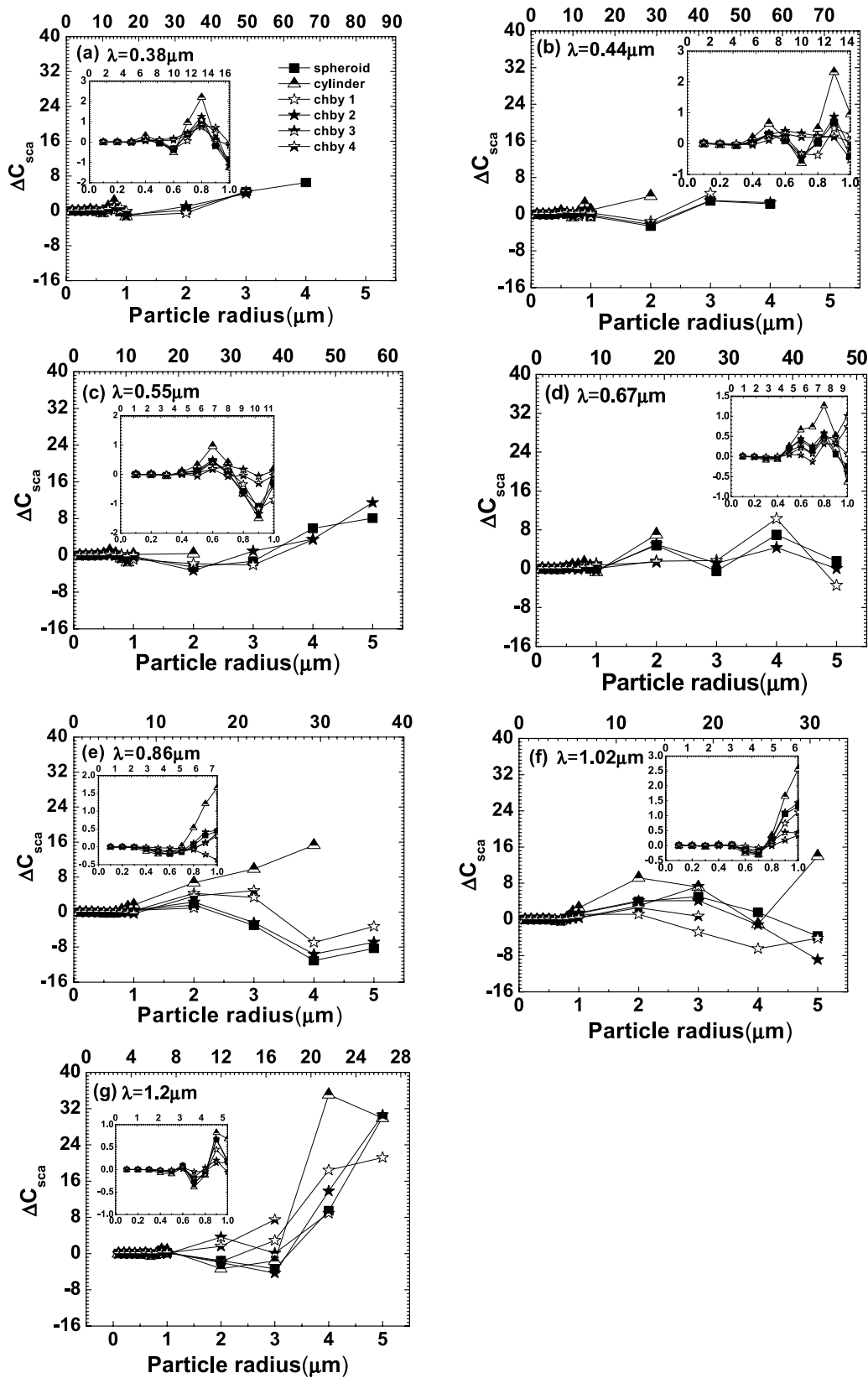
Figure 6. Difference in scattering cross-section between nonsphere and sphere, ΔC_{sca}, for 0% hematite as a function of particle radius at wavelength (a) 0.38, (b) 0.44, (c) 0.55, (d) 0.67, (e) 0.86, (f) 1.02, and (g) 1.2 μm. The top x axis in each plot represents the size parameter α. The inset in the subfigures shows the same variation but for particle radius <1 μm.
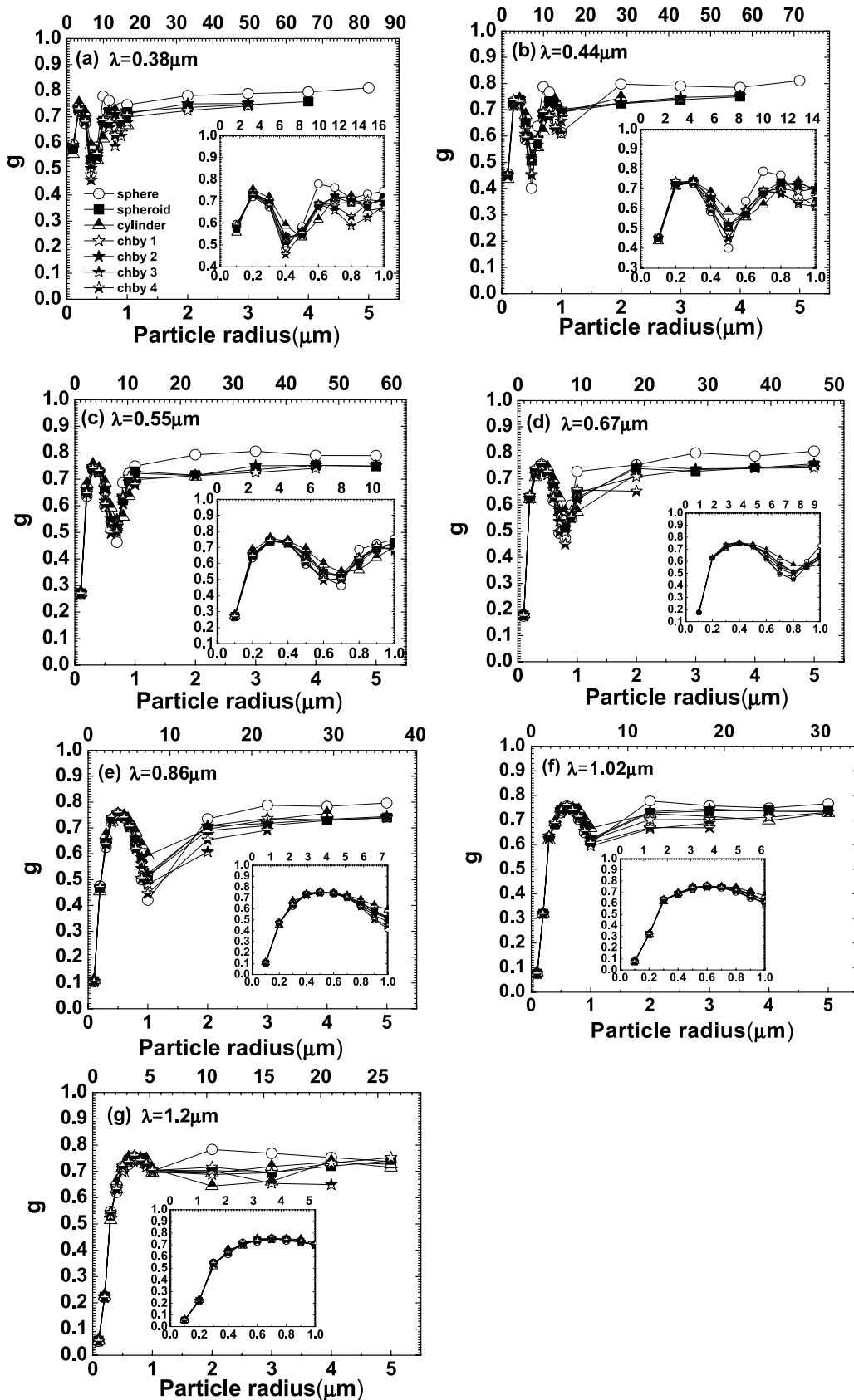
Figure 7. Asymmetry parameter, g, variation of dust for 0% hematite as a function of particle radius at wavelength (a) 0.38, (b) 0.44, (c) 0.55, (d) 0.67, (e) 0.86, (f) 1.02, and (g) 1.2 μm. The top x axis in each plot represents the size parameter α. The inset in the subfigures shows the same variation but for particle radius <1 μm.

that the difference in SSA for nonspherical particles to that of spherical ones decreases with increasing wavelength. The deviation in SSA of nonspherical particles to that of spherical one is clearly visible at 0.86 μm for $\alpha \geq 5$. The numerical study by *Pollack and Cuzzi* [1980] has also shown similar results for $\alpha > 5$.

[26] Figure 6 presents the difference between scattering cross-section of nonspherical particle and spherical ones, ΔC_{sca}, for the same dust composition as in Figure 5. Insets have been used in the figure for particles with radius <1 μm. From Figure 6a, for the ultraviolet regime, the smooth shape particles (chby1, chby2 and spheroid) show slight deviation from equivalent sphere up to $\alpha = 33$ which increases with increase in size. T-matrix code could not converge for any nonspherical particle for $\alpha \geq 83$. The inset for the figure reveals that, for $\alpha \geq 5$, the nonspherical particles show a slight deviation from spherical one unto $\alpha = 10$ while beyond this a noticeable deviation is seen. Figures 6b, 6c and 6d depict that the scattering cross-section of nonspherical particles is higher compared to their equivalent sphere generally. T-matrix code could converge only for particles chby1, chby2, chby4, spheroid and cylinder with particle radius >1 μm for visible wavelength domain. The insets for the above figure show that, for $\alpha \geq 2$–4, in general, the nonspherical particles show high scattering cross-section to that of spherical one in the visible wavelength domain. Sharp-edged cylindrical particles show significant deviation to that of volume equivalent spheres with increasing particle size. Figures 6e, 6f and 6g, for the infrared regime, shows that the difference in scattering cross-section area of nonspherical to spherical enhances with particle size. In the infrared regime, T-matrix code could converge for all shapes but not for the entire particle size range, so up to certain size we can see the variation of other particles. Even, in this regime, particles with radius >1 μm did not show any regular pattern while the insets in Figures 6e, 6f and 6g, for $\alpha \leq 1.6$–3, depict that the nonspherical particles show nearly the same scattering pattern as that of equivalent spheres but beyond that the former one shows large scattering relative to that of equivalent spheres. The sharp-edged cylindrical particle shows similar behavior as seen in previous plots. Overall, Figure 6 shows that the scattering pattern of nonspherical particles is nearly the same to that of equivalent spheres for particle radius <1 μm while it deviates to the later for particle radius >1 μm.

[27] The scattering features of the mineral dust particles support the variation of SSA with particle size as shown in Figure 5. Past studies [*Pollack and Cuzzi*, 1980; *Mugnai and Wiscombe*, 1986] demonstrated that the nonspherical particles possess higher scattering cross-section compared to that of volume equivalent spheres beyond a critical size parameter. On the basis of the numerical study by *Greenberg* [1972], extinction efficiency of stacked cylinders was found to be deviating more from that of volume equivalent spherical counterpart with increasing particle size for a

given refractive index and wavelength whereas deviation in absorption efficiency was insignificant. For small particle size, the extinction cross-section depends strongly on particle volume than on the particle shape.

[28] The radiative forcing calculations are made computationally efficient by representing aerosol angular scattering in a single quantity such as asymmetry parameter, g, that cannot be measured directly and is an important input in radiative transfer models. Values of g vary from -1 to $+1$ for complete backward and forward scattering, respectively. Model results suggest that a 10% reduction in g leads to 19% reduction of aerosol radiative forcing at the top of atmosphere while at the surface it is 13% [*Ogren et al.*, 2006]. Figure 7 shows the asymmetry parameter for the mineral dust particles for 0% hematite. In Figure 7a, for the ultraviolet regime, T-matrix code could converge only for chby1, chby2 and spheroid so we could not get complete information on the effect of particle nonsphericity on g for particle radius >1 μm. However, particles with radius <1 μm, in the inset, show that for $\alpha \leq 3$, there occurs negligible difference in g of nonspherical and its spherical counterpart but beyond this the difference becomes significant. For the visible wavelength domain, Figures 7b, 7c and 7d, show that the equivalent spheres overestimate g values for the particle radius >1 μm. On the other hand, the insets in Figures 7b, 7c and 7d depict that for $\alpha \geq 4$–4.6, the variation of g of the particles follow the sinusoidal (cyclic) pattern in which the first half of the cycle shows larger g values for nonspherical particles compared to that of volume equivalent sphere while for the second half reverse is true with increasing size. The deviation in g of nonspherical particles to that of equivalent sphere is significant for the above threshold value of α, below which the deviation is negligible. In the infrared regime, Figures 7e, 7f and 7g, T-matrix code converged for all shapes with increasing wavelength for particle radius >1 μm but not for the entire size range. No regular pattern could be observed for above size range whereas for particles with radius <1 μm in the insets of Figures 7e, 7f and 7g show that, for $\alpha \geq 4.2$–5, difference between nonspherical and volume equivalent spherical particle diminishes with increasing wavelength. Also, in the above insets, an increase in g of the particles has been noted for the increasing wavelength for large size particles in the infrared regime. In a nutshell, Figure 7 depicts a strong variation in g with particle radius <1 μm while beyond this size this variation diminishes. The effect of particle nonsphericity on g is stronger for particles of radius >1 μm compared to those <1 μm.

[29] The earlier computational work pertaining to spheroidal particle optics [*Asano and Sato*, 1980] discussed the fact that beyond a certain size parameter, g of spheroid is greater than that of volume equivalent spheres. The results based on the study of nonspherical Chebyshev particles [*Mugnai and Wiscombe*, 1986] found relatively low value of g for nonspherical particle than that of volume equivalent

Figure 8. SSA for 2% hematite as a function of particle radius at wavelength (a) 0.38, (b) 0.44, (c) 0.67, and (d) 1.02 μm. ΔC_{sca} for 2% hematite as a function of particle radius at wavelength (e) 0.38, (f) 0.44, (g) 0.67, and (h) 1.02 μm. The top x axis in each plot represents the size parameter α. The inset in the subfigures shows the same variation but for particle radius <1 μm.
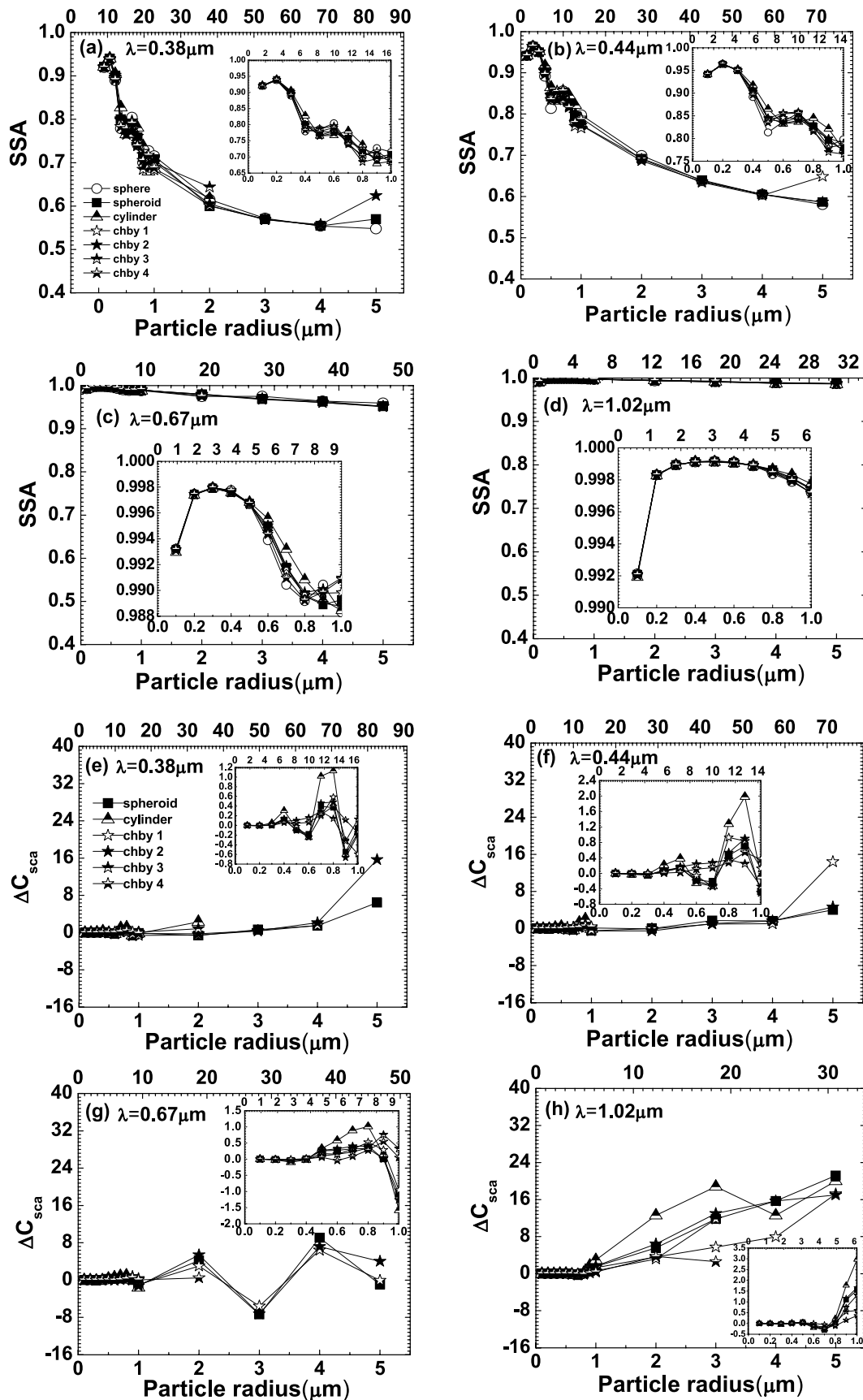
Figure 8

Figure 9. SSA for 4% hematite as a function of particle radius at wavelength (a) 0.38, (b) 0.44, (c) 0.67, and (d) 1.02 μm. ΔC_{sca} for 4% hematite as a function of particle radius at wavelength (e) 0.38, (f) 0.44, (g) 0.67, and (h) 1.02 μm. The top x axis in each plot represents the size parameter α. The inset in the subfigures shows the same variation but for particle radius <1 μm.
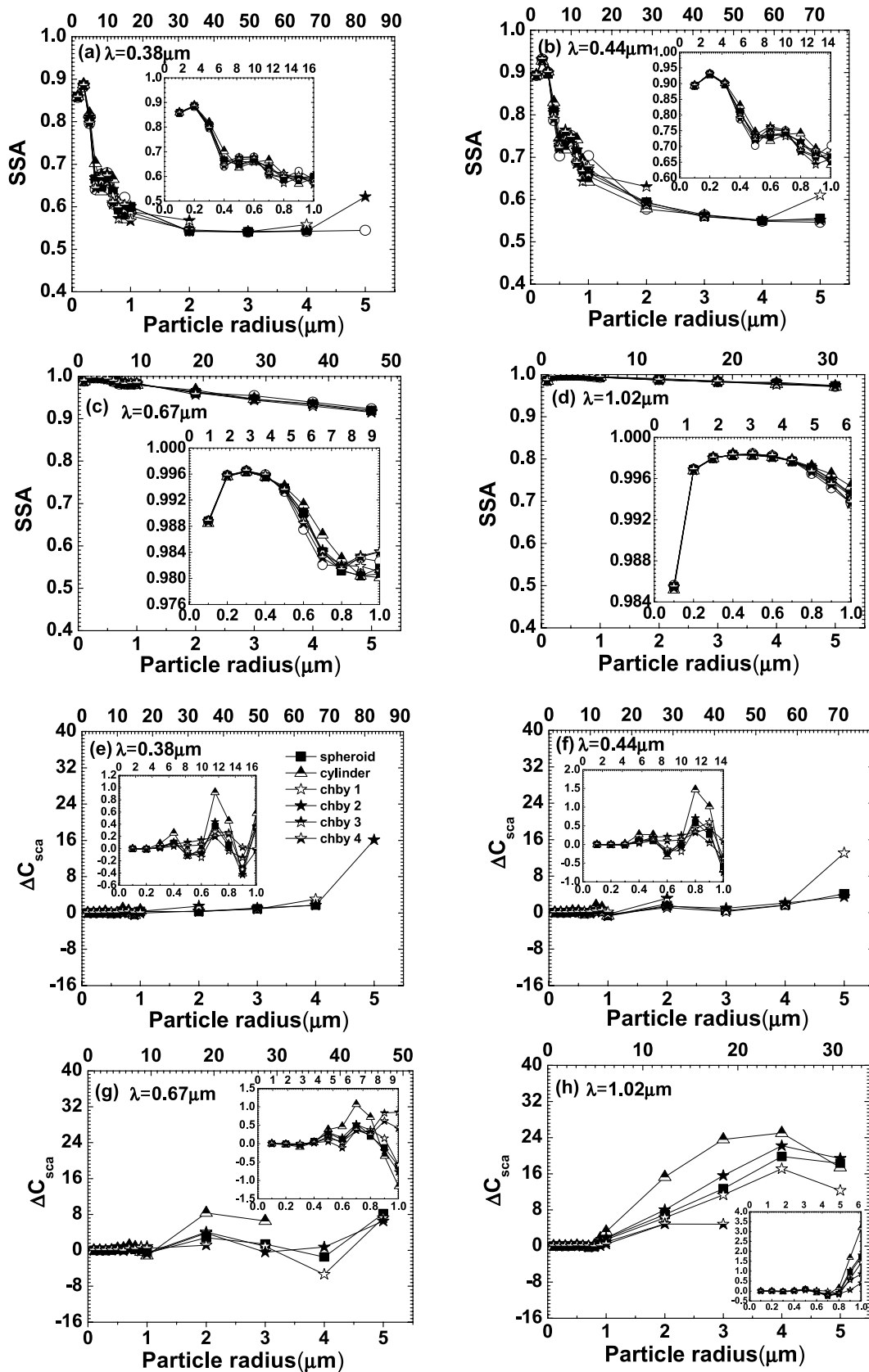
Figure 10. SSA for 6% hematite as a function of particle radius at wavelength (a) 0.38, (b) 0.44, (c) 0.67, and (d) 1.02 μm. ΔC_{sca} for 6% hematite as function of particle radius at (e) wavelength, 0.38, (f) 0.44, (g) 0.67, and (h) 1.02 μm. The top x axis in each plot represents the size parameter α. The inset in the subfigures shows the same variation but for particle radius <1 μm.
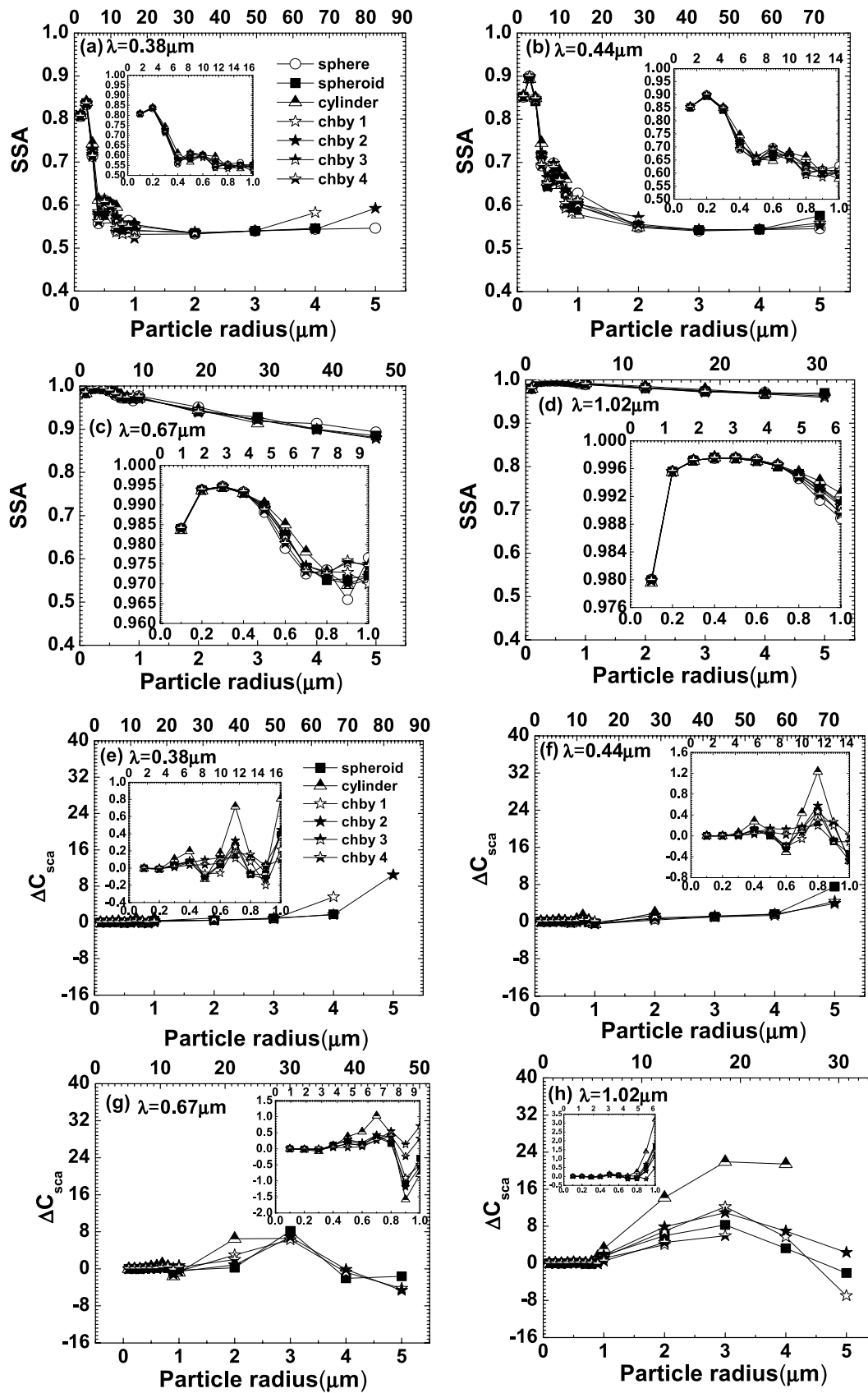
Figure 11. SSA for 8% hematite as a function of particle radius at wavelength (a) 0.38, (b) 0.44, (c) 0.67, and (d) 1.02 μm. ΔC_{sca} for 8% hematite as a function of particle radius at wavelength (e) 0.38, (f) 0.44, (g) 0.67, and (h) 1.02 μm. The top x axis in each plot represents the size parameter α. The inset in the subfigures shows the same variation but for particle radius <1 μm.
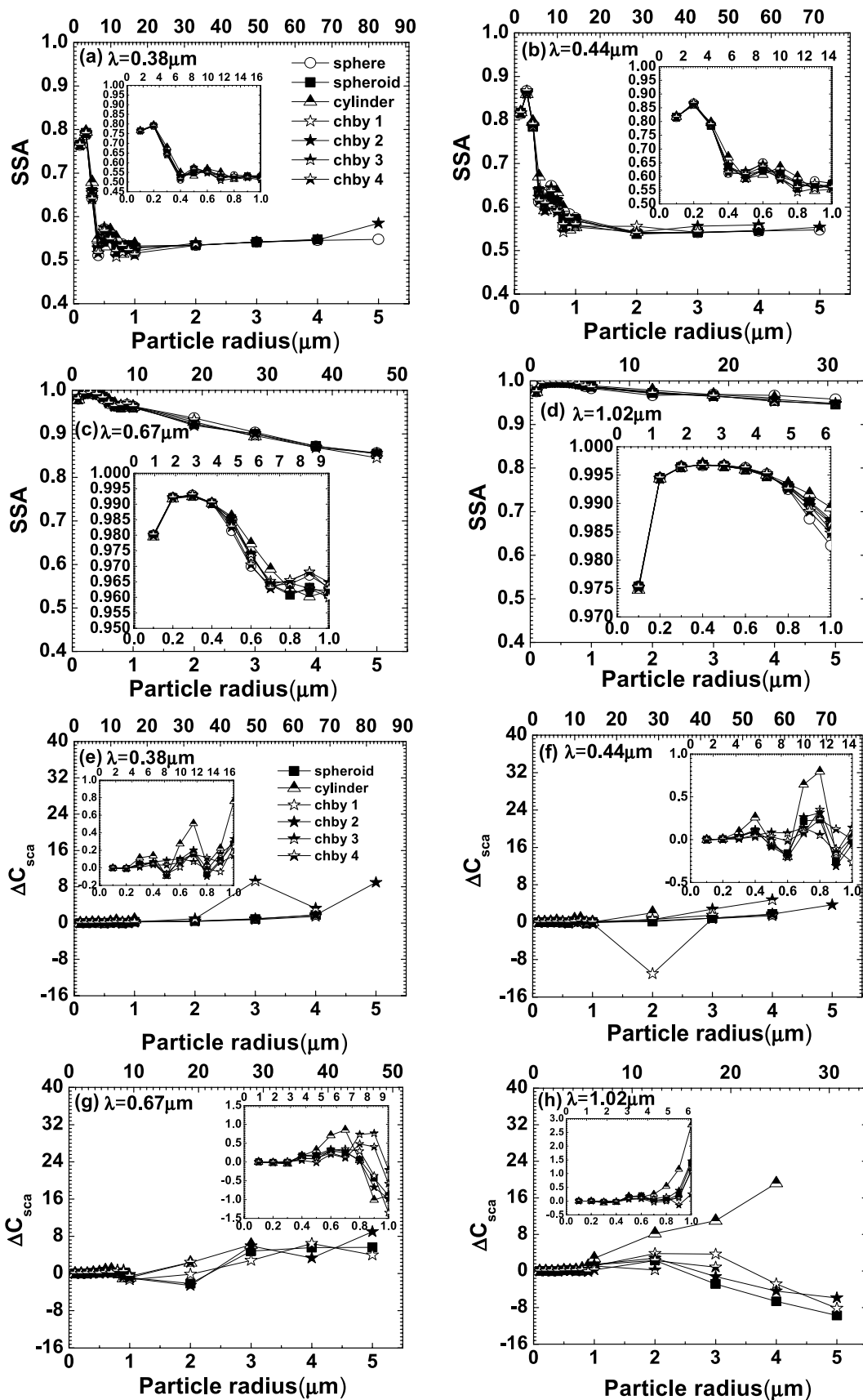
Table 2. Reduction in SSA for Spherical and Nonspherical Particle for Particle Radius 1 μm at Different Wavelengths When Hematite Fraction was Increased From 0% to 10%

Wavelength (μm)	Reduction in SSA	
	Spherical Particle	Cylindrical Particle
0.38	0.484	0.477
0.44	0.455	0.462
0.67	0.044	0.044
1.02	0.022	0.013

sphere for $8 \leq \alpha \leq 15$. The results of g, in the present study, follow the same pattern for the entire wavelength domain except at 0.44 μm. The study by *Pollack and Cuzzi* [1980] also shows lower value of g for irregular tropospheric particles compared to that of equivalent sphere.

[30] The absorption was found to be negligible for the mineral dust with only nonmetallic component. The absorptive nature of the dust can be seen either due to mixing of pure dust with absorbing pollutants such as black carbon etc. or presence of hematite as mineral dust component. To gain the realistic scattering signature of the mineral dust over the Indian Desert, hematite percentage has been varied from 2–10% and for each case dust particle optics has been modeled. Here we show some important optical properties such as C_{sca}, and SSA at 4 selected wavelengths. The results for g are not shown here.

[31] Figure 8 shows modeled optical properties (SSA and C_{sca}) for the dust with 2% hematite and 98% nonmetallic composition for four wavelengths namely, 0.38, 0.44, 0.67 and 1.02 μm and the same has been shown in the inset for the particles with radius <1 μm. Figures 9, 10, 11 and 12 show the same modeled optical properties of dust at the same wavelengths as in Figure 8 but for 4%, 6%, 8% and 10% hematite, respectively. Comparing SSA of the dust particles in Figures 5, 8, 9, 10, 11 and 12, the sharp reduction in SSA is quiet evident with increasing hematite percentage. Comparing Figures 5, 8, 9, 10, 11 and 12, we find that the SSA variation with particle size is flattened at 0.38 and 0.44 μm wavelength with increasing hematite percentage in the mineral dust while it declines sharply at 0.67 μm with minor decrease at 1.02 μm wavelengths. The relative change in SSA, for 4–10% hematite, with particle size is significant for particles with radius <1 μm compared to that for particles with >1 μm radius at 0.38 and 0.44 μm wavelengths. For particles >1 μm, we could not trace any regular pattern for SSA and ΔC_{sca} because of the convergence issue of T-matrix code for several shapes. Table 2 shows the effect of variation of hematite from 0 to 10% in mineral dust composition on SSA at different wavelength for cylindrical particle and equivalent spherical particle with radius 1 μm.

[32] The nonspherical mineral dust particles are a significant fraction of total dust loading during dust storms. However, the presence of relatively lesser fraction of nonspherical particles cannot be ignored in background dust. *Parungo et al.* [1997] suggested the background dust composition as 20% spheres, 50% sharp-edged, and remaining smooth shapes (SC1) particles while the same for the dust storm as 5% spheres, 70% sharp-edged, and remaining 25% smooth shapes (SC2) particles over the Asian region.

[33] Figure 13 shows the effective SSA as a function of particle radius for the background dust composition (SC1) and that for dust storm (SC2). Figure 13 reveals that the reduction in SSA is greater than 0.2 for the increase of hematite from 0 to 6% for both background dust and dust storm cases for 1 μm size particle at 0.55 μm wavelength. The above reduction in SSA cannot be ignored as earlier study by *Hansen et al.* [1997] shows that a moderate change in the SSA from 0.90 to 0.80 can change its radiative forcing from negative to positive at TOA. The change in SSA is insignificant between background dust and dust storm cases for particles of size <0.4 μm for each hematite percentage. While beyond this size, the SSA change becomes prominent with increasing hematite percentage. The SSA change of ~0.01 has been seen between the background dust and dust storm case for 1 μm size particle for 6% hematite. Although the above change in SSA is small but not ignorable. In general, for the particle size range (up to 1 μm particle size), the SSA of the mineral dust was found to be increasing during dust storm over the desert compared to that of background dust for all the cases considered in the figure.

[34] T-matrix method for calculations of the optical properties of polydisperse dust distribution has been tested and verified with *Mishchenko et al.* [2005, 284 pp.]. Selected optical properties such as SSA and g have been calculated for polydisperse dust with lognormal distribution for median radius, r = 0.5 μm and a geometric standard deviation, σ = 1.5 [*Dubovik et al.*, 2000; *Reid et al.*, 2003a, 2003b] at λ = 0.55 μm. Here the hematite percentage has been varied from 0 to 10% in the dust. The modeled dust shapes were sphere, spheroid and cylinder. The calculated SSA and g are summarized in Table 3. On the basis of Table 3, the SSA range of 0.88–0.94 inferred by *Moorthy et al.* [2007] in the visible region corresponds to hematite percentage 0 to 4% in the mineral desert dust. Dust at the source can be considered purer compared to the dust transported to long distance where mixing of dust with anthropogenic pollutants such as black carbon occurs. The low SSA of the desert dust over the desert by Moorthy et al. may be because of the above hematite percentage and not due the mixing of dust with black carbon. On increasing the hematite percentage from 0 to 10% in the dust, the SSA of the dust was found to be reduced while g was found to be increased. The effect of hematite variation on SSA is more than that of nonsphericity for a given hematite percentage in the dust (Table 3).

[35] *Chinnam et al.* [2006] predicted low SSA using the composite aerosol (incorporating dust) model during the dust storm in Kanpur. However low SSA has been reported due to mixing of dust aerosol with black carbon during transportation of dust from source regions. In this study, the dust contribution to the net TOA and surface forcing were found to be +7 and −12 Wm^{-2}. Another study made by *Dey et al.* [2004] highlighted the effect of dust storms on the local atmospheric aerosol optics. An enhancement in AOD by more than 50% has been registered during the dust storm. The SSA, modeled in the present study for the background dust (SC1) and dust storm (SC2) for 0−6% hematite as a function of particle radius at λ = 0.55 μm matches with the study by Dey et al. where during the dust
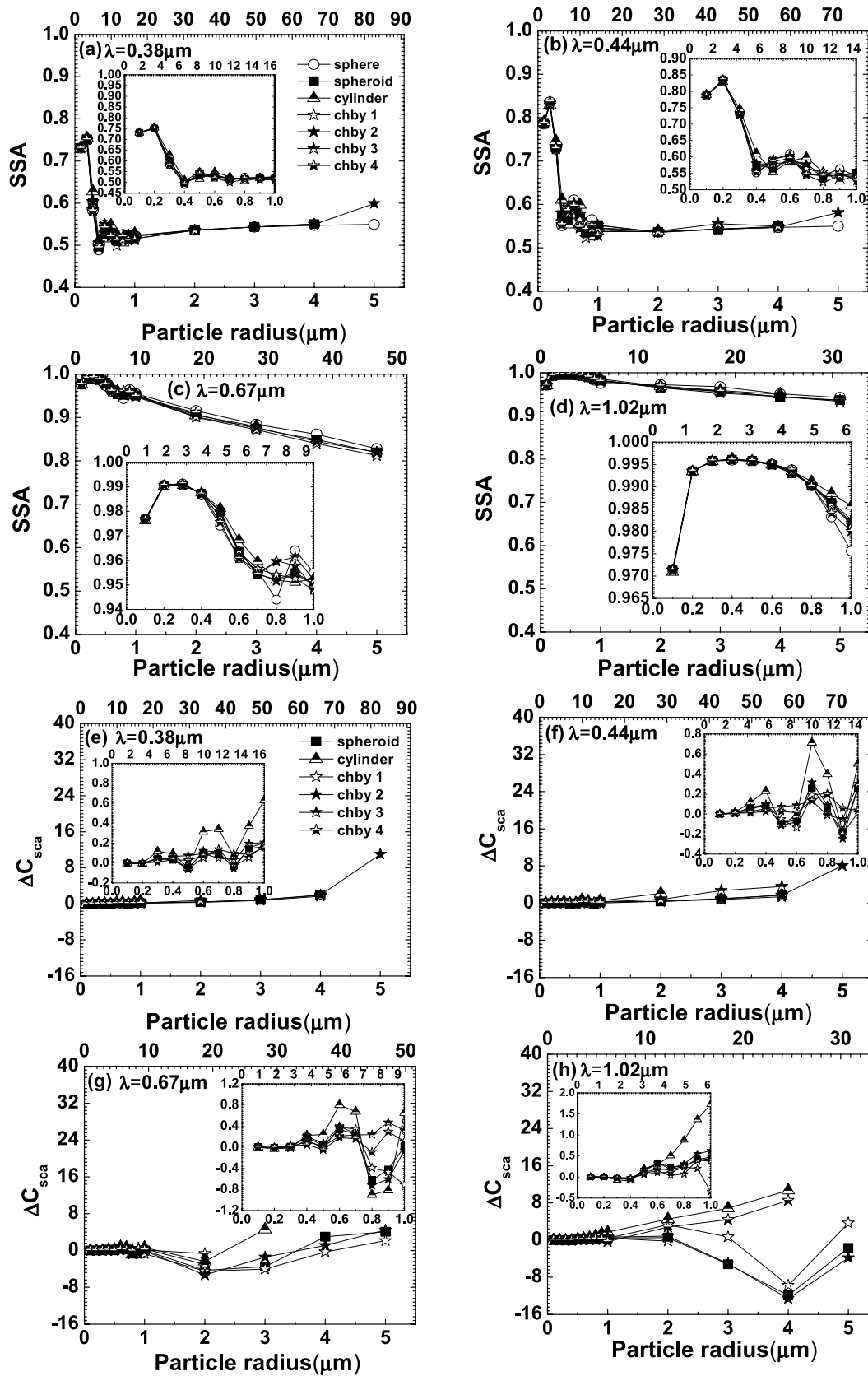
Figure 12. SSA for 10% hematite as a function of particle radius at wavelength (a) 0.38, (b) 0.44, (c) 0.67, and (d) 1.02 μm. ΔC_{sca} for 10% hematite as a function of particle radius at wavelength (e) 0.38, (f) 0.44, (g) 0.67, and (h) 1.02 μm. The top x axis in each plot represents the size parameter α. The inset in the subfigures shows the same variation but for particle radius <1 μm.

events, increase in SSA values has been reported at higher wavelength (>0.4 μm). Dey et al. have also reported the Thar desert as the source of the dust transporting by southwesterly wind to Kanpur.

6. Conclusions

[36] 1. The sharp-edged cylindrical particle with radius (>0.6 μm) showed largest deviation from the equivalent sphere compared to that of relatively smooth particles such as spheroid and Chebyshev for all optical properties. The reduction in SSA for cylindrical particle of radius 1 μm was found to be 0.4772 and 0.0131 at ultraviolet and near infrared, respectively, whereas for volume equivalent spherical particle it was 0.4840 and 0.0227 on increasing the hematite percentage from 0 to 10 in the mineral dust.

[37] 2. SSA for the background dust and dust storm case has been studied; the reduction in SSA is greater than 0.2 for the increase of hematite from 0 to 6% for both background dust and dust storm cases for 1 μm size particle at 0.55 μm wavelengths. The change in SSA between background dust and dust storm cases for particles of size <0.4 μm is insignificant for each hematite percentage, considered. Beyond this size, the change in SSA becomes significant with increasing hematite percentage. The SSA change of ~0.01 has been seen between the background dust and dust storm case for 1 μm size particle for 6% hematite. Consideration of more complicated nonspherical particles in the computations may lead to significant difference in SSA between above two cases.

[38] 3. SSA range of 0.88−0.94 inferred by *Moorthy et al.* [2007] in the visible region corresponds to hematite percentage of 0−4% in the mineral desert dust. At the source, dust may be absorbing because of the above hematite percentage. Increase of hematite percentage from 0 to 10% in the dust lead the reduced SSA and enhanced g
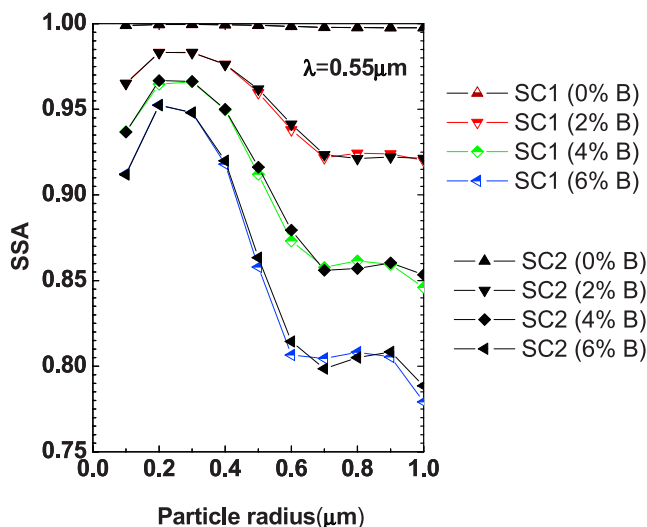
Table 3. Effect of Hematite Variation (0%−10%) and Nonsphericity on SSA and g of the Dust at $\lambda = 0.55$ μm[a]

Hematite (%)	Sphere		Spheroid		Cylinder	
	SSA	g	SSA	g	SSA	g
0	0.997	0.619	0.997	0.562	0.997	0.561
2	0.915	0.651	0.921	0.624	0.919	0.584
4	0.871	0.766	0.861	0.684	0.850	0.622
6	0.833	0.791	0.810	0.731	0.792	0.668
8	0.789	0.804	0.768	0.772	0.751	0.724
10	0.759	0.822	0.735	0.798	0.727	0.769

[a]Optical properties have been averaged over a log-normal size distribution, with $r = 0.5$ μm and $\sigma = 1.5$.

of the dust. The dust SSA is more sensitive to hematite percentage compared to particle nonsphericity.

[39] 4. The retrieval of aerosol optical properties using satellite radiances requires an *a priori* aerosol model for the region which provides aerosol scattering phase function and SSA etc. [*Wang and Gordon*, 1994]. In general these aerosol models estimate the optical properties of the dust particles by assuming them to be spherical and/or a combination of sphere and spheroid leading to inaccurate retrievals. To overcome such issues, accurate region specific dust optical models are required. Laboratory experiments are another route but difficult to implement [*Kuik et al.*, 1991; *West et al.*, 1997; *Minoz et al.*, 2001; *Volten et al.*, 2001]. Therefore numerical modeling of the dust optics is probably the best way to deal with the problem related to particle nonsphericity.

[40] 5. In the present study, we performed extensive calculations of region specific mineral dust optics over the Indian Desert for the first time. The likely hematite percentage in the mineral dust has been deduced. The modeled optical properties for the inferred hematite percentage may be used to improve upon the existing satellite retrieval algorithms. Accounting hematite percentage and nonsphericity will also improve the forcing imposed by the mineral dust over the Indian Desert.

[41] 6. The changes in mineral dust optics because of sharp-edged nonspherical particles during background dust and dust storm cases can be better studied by considering more nonspherical shapes which could not be taken in the present study because of the limitations of T-matrix method. The T-matrix method to calculate optical properties for all particle shapes over the entire size range of mineral dust particles is not sufficient. It leads to the additional uncertainty regarding the results for larger particle sizes. The cluster of particles, which are not incorporated in the present computations, may add some additional uncertainty to modeled dust optical properties.

Figure 13. Effective single scattering albedos (SSA) for the background dust (SC1) and dust storm (SC2) have been shown for hematite variation from 0% to 6% as a function of particle radius at 0.55 μm. SC1 and SC2 have been described in the text. The quantity in bracket is the volume percentage of the metallic component (B).

References

Anderson, J. R., P. R. Busek, and T. L. Patterson (1992), Characterization of individual fine-fraction particles from the Arctic aerosol at Spitsbergen, May−June 1987, *Atmos. Environ.*, *26A*, 1747−1762.

Asano, S., and G. Yamamoto (1975), Light scattering by a spheroidal particle, *Appl. Opt.*, *14*, 29−49.

Asano, S., and M. Sato (1980), Light scattering by randomly oriented spheroidal particles, *Appl. Opt.*, *19*, 962−974.

Bishop, J. K. B., R. E. Davis, and J. T. Sherman (2002), Robotic observations of dust storm enhancement of carbon biomass in the North Pacific, *Science*, *298*(5594), 817–821.

Bohren, C. F., and D. R. Huffman (1998), *Absorption and Scattering of Light by Small Particles*, John Wiley Inc., New York.

Carlson, T. N., and R. S. Caverly (1977), Radiative characteristics of Saharan dust at solar wavelengths, *J. Geophys. Res.*, *82*, 3141–3152.

Chinnam, N., S. Dey, S. N. Tripathi, and M. Sharma (2006), Dust events in Kanpur, northern India: Chemical evidence for source and implications to radiative forcing, *Geophys. Res. Lett.*, *31*, L08803, doi:10.1029/2005GL025278.

Choi, J. C., M. Lee, Y. Chun, J. Kim, and S. Oh (2001), Chemical composition and source signature of spring aerosol in Seoul, Korea, *J. Geophys. Res.*, *106*, 18,067–18,074.

Collins, W. D., P. J. Rasch, B. E. Eaton, B. V. Khattatov, J. F. Lamarque, and C. S. Zender (2001), Simulating aerosols using a chemical transport model with assimilation of satellite aerosol retrievals: Methodology for INDOEX, *J. Geophys. Res.*, *106*, 7313–7336.

Dave, J. V. (1968), Subroutines for computing the parameters of the electromagnetic radiation scattered by spheres, *Rep. 320-3237*, IBM Palo Alto Scientific Center, Palo Alto, Calif.

Deepshikha, S., et al. (2005), Regional distribution of absorbing efficiency of dust aerosols over India and adjacent continents, *Geophys. Res. Lett.*, *32*, L03811, doi:10.1029/2004GL022091.

Dey, S., S. N. Tripathi, and R. P. Singh (2004), Influence of dust storms on the aerosol optical properties over the Indo-Gangetic basin, *J. Geophys. Res.*, *109*, D20211, doi:10.1029/2004JD004924.

Dubovik, O., A. Smirnov, B. Holben, M. D. King, Y. J. Kaufman, T. F. Eck, and I. Slutsker (2000), Accuracy assessments of aerosol optical properties retrieved from aerosol robotic network (AERONET) sun and sky radiance measurements, *J. Geophys. Res.*, *105*, 9791–9806.

Dubovik, O., B. Holben, T. F. Eck, A. Smirnov, Y. J. Kaufman, M. D. King, D. Tanré, and I. Slutsker (2002), Variability of absorption and optical properties of key aerosol types observed in world wide locations, *J. Atmos. Sci.*, *59*, 590–608.

Dubovik, O., et al. (2006), Application of spheroid models to account for aerosol particle nonsphericity in remote sensing of desert dust, *J. Geophys. Res.*, *111*, D11208, doi:10.1029/2005JD006619.

Egan, W. G., and T. W. Hilgeman (1979), *Optical Properties of Inhomogeneous Materials*, Academic, San Diego, Calif.

Forster, P., et al. (2007), Changes in atmospheric constituents and in radiative forcing, in *Climate Change 2007: The Physical Science Basis. Contribution of Working Group I to the Fourth Assessment Report of the Intergovernmental Panel on Climate Change*, Cambridge Univ. Press, Cambridge, New York.

Ginoux, P., M. Chin, I. Tegen, J. Prospero, B. Holben, O. Dubovik, and S. J. Lin (2001), Sources and distributions of dust aerosols simulated with the GOCART model, *J. Geophys. Res.*, *106*, 20,255–20,273.

Goudie, A. S. (1978), Dust storms and their geomorphological implications, *J. Arid Environ.*, *1*, 291–310.

Greenberg, J. M. (1972), Absorption and emission of radiation by nonspherical particles, *J. Colloid Interface Sci.*, *39*, 513–519.

Hansen, J., M. Sato, and R. Ruedy (1997), Radiative forcing and climate response, *J. Geophys. Res.*, *102*, 6831–6864.

Harrison, E. F., P. Minnis, B. R. Barkstrom, V. Ramanathan, R. D. Cess, and G. G. Gibson (1990), Seasonal variation of cloud radiative forcing derived from the earth radiation budget experiment, *J. Geophys. Res.*, *95*, 18,687–18,703.

Haywood, J. M., and O. Boucher (2000), Estimates of the direct and indirect radiative forcing due to tropospheric aerosols: A review, *Rev. Geophys.*, *38*(4), 513–543.

Haywood, J. M., P. N. Francis, M. D. Glew, O. Dubovik, and B. N. Holben (2003a), Comparison of aerosol size distributions, radiative properties, and optical depths determined by aircraft observations and Sun photometers during SAFARI-2000, *J. Geophys. Res.*, *108*(D13), 8471, doi:10.1029/2002JD002250.

Haywood, J. M., et al. (2003b), Radiative properties and direct radiative effect of Saharan dust measured by the C-130 aircraft during SHADE. 1: Solar spectrum, *J. Geophys. Res.*, *108*(D18), 8577, doi:10.1029/2002JD002687.

Highwood, E. J., J. M. Haywood, M. D. Silverstone, S. M. Newman, and J. P. Taylor (2003), Radiative properties and direct effect of Saharan dust measured by the C-130 aircraft during SHADE. 2: Terrestrial spectrum, *J. Geophys. Res.*, *108*(D18), 8578, doi:10.1029/2002JD002552.

Houghton, J., Y. Ding, D. J. Griggs, M. Noguer, P. J. van der Linden, and E. Xiaosu (2001), *Climate Change 2001: The Scientific Basis: Contributions of Working Group I to the Third Assessment Report of the Intergovernmental Panel on Climate Change*, Cambridge Univ. Press, New York.

Hsu, N. C., J. R. Herman, and C. Weaver (2000), Determination of radiative forcing of Saharan dust using combined TOMS and ERBE data, *J. Geophys. Res.*, *105*, 20,649–20,661.

Ivlev, L. S., and S. I. Popova (1973), The complex refractive indices of substances in the atmospheric aerosol dispersed phase, *Izv. Atmos. Oceanic Phys.*, *9*, 587–591.

Kalashnikova, O. V., and I. N. Sokolik (2002), Importance of shapes and compositions of wind-blown dust particles for remote sensing at solar wavelengths, *Geophys. Res. Lett.*, *29*(10), 1398, doi:10.1029/2002GL014947.

Kalashnikova, O. V., and I. N. Sokolik (2004), Modeling the radiative properties of nonspherical soil-derived mineral aerosols, *J. Quant. Spectrosc. Radiat. Transfer*, *87*, 137–166.

Kaufman, Y. J., D. Tanre, O. Dubovik, A. Karnieli, and L. A. Remer (2001), Absorption of sunlight by dust as inferred from satellite and ground-based remote sensing, *Geophys. Res. Lett.*, *28*, 1479–1483.

Koven, C. D., and I. Fung (2006), Inferring dust composition from wavelength-dependent absorption in Aerosol Robotic Network (AERONET) data, *J. Geophys. Res.*, *111*, D14205, doi:10.1029/2005JD006678.

Kubilay, N., T. Cokacar, and T. Oguz (2003), Optical properties of mineral dust outbreaks over the northeastern Mediterranean, *J. Geophys. Res.*, *108*(D21), 4666, doi:10.1029/2003JD003798.

Kuik, F., P. Stammes, and J. W. Hovenier (1991), Experimental determination of scattering matrices of water droplets and quartz particles, *Appl. Opt.*, *30*, 4872–4881.

Lafon, S., J. L. Rafot, S. C. Alfaro, L. Gomes, M. Maill, and A. Gaudichet (2001), Iron status in mineral desert aerosols, in *IAMAS Congress No. 2 in 5*, AMS, Innsbruck.

Lafon, S., I. N. Sokolik, J. L. Rajot, S. Caquineau, and A. Gaudichet (2006), Characterization of iron oxides in mineral dust aerosols: Implications for light absorption, *J. Geophys. Res.*, *111*, D21207, doi:10.1029/2005JD007016.

Liao, H., and J. H. Seinfeld (1998), Radiative forcing by mineral dust aerosols: Sensitivity to key variables, *J. Geophys. Res.*, *103*, 31,637–31,645.

Long, L. L., M. R. Querry, R. J. Bell, and R. W. Alexander (1993), Optical properties of calcite and gypsum in crystalline and powdered form in the infrared and far-infrared, *Infrared Phys.*, *34*, 191–201.

Meenakshy, V., and S. Sadasivan (1993), Air quality measurement at Gurushikar, Mt. Abu, in *Proc. 2nd National Symposium on Environment*, Jodhpur, India, 27–30 Jan.

Miller, R. L., and I. Tegen (1998), Climate response to soil dust aerosols, *J. Clim.*, *11*, 3247–3267.

Miller, R. L., et al. (2006), Mineral dust aerosols in the NASA Goddard Institute for Space Sciences ModelE atmospheric general circulation model, *J. Geophys. Res.*, *111*, D06208, doi:10.1029/2005JD005796.

Minoz, O., H. Volten, J. Haan, W. Vassen, and J. Hovenier (2001), Experimental determination of scattering matrices of randomly oriented fly ash at 442 and 633 nm, *J. Geophys. Res.*, *106*, 22,833–22,845.

Mishchenko, M. I., and L. D. Travis (1998), Capabilities and limitations of a current FORTRAN implementation of the T-matrix method for randomly oriented, rotationally symmetric scatterers, *J. Quant. Spectrosc. Radiat. Transfer*, *60*, 309–324.

Mishchenko, M. I., et al. (1997), Modeling phase functions for dustlike tropospheric aerosols using a shape mixture of randomly oriented polydisperse spheroids, *J. Geophys. Res.*, *102*, 16,831–16,847.

Mishchenko, M. I., L. D. Travis, and A. A. Lacis (2005), *Scattering, Absorption, and Emission of Light by Small Particles*, 2nd electronic ed., NASA Goddard Institute for Space Studies, New York.

Moorthy, K. K., S. Suresh Babu, S. K. Satheesh, J. Srinivasan, and C. B. S. Dutt (2007), Dust absorption over the "Great Indian Desert" inferred using ground-based and satellite remote sensing, *J. Geophys. Res.*, *112*, D09206, doi:10.1029/2006JD007690.

Mugnai, A., and W. J. Wiscombe (1986), Scattering from nonspherical Chebyshev particles. Cross sections, single-scattering albedos, asymmetry factor, and backscattered fraction, *Appl. Opt.*, *25*, 1235–1244.

Myhre, G., and F. Stordal (2001), Global sensitivity experiments of the radiative forcing due to mineral aerosols, *J. Geophys. Res.*, *106*, 18,193–18,204.

Myhre, G., A. Grini, J. M. Haywood, F. Stordal, B. Chatenet, D. Tanré, J. K. Sundet, and I. S. A. Isaksen (2003), Modelling the radiative impact of mineral dust during the Saharan Dust Experiment (SHADE) campaign, *J. Geophys. Res.*, *108*(D18), 8579, doi:10.1029/2002JD002566.

Negi, B. S., S. Sadasivan, K. S. V. Nambi, and B. M. Pande (1996), Characterization of atmospheric dust at Gurushikar, Mt. Abu, Rajasthan, *Environ. Monit. Assess.*, *40*, 253–259.

Negi, B. S., S. K. Jha, S. B. Chavan, S. Sadasivan, A. Goyal, M. L. Sapru, and C. L. Bhat (2002), Atmospheric dust loads and their elemental composition at a background site in India, *Environ. Monit. Assess.*, *73*, 1–6.

Nousiainen, T., and K. Vermeulen (2003), Comparison of measured single scattering matrix of feldspar particles with T-matrix simulations using spheroids, *J. Quant. Spectrosc. Radiat. Transfer*, *79*, 1031–1042.

Ogren, J. A., E. Andrews, A. McComiskey, P. Sheridan, A. Jefferson, and M. Fiebig (2006), New insights into aerosol asymmetry parameter, in *Sixteenth ARM Science Team Meeting Proceedings*, Albuquerque, N. M., 27–31 Mar.

Okada, K., J. Heintzenberg, K. Kai, and Y. Qin (2001), Shape of atmospheric mineral particles collected in three Chinese arid-regions, *Geophys. Res. Lett.*, *28*, 3123–3126.

Palik, E. D. (1985), *Handbook of Optical Constants of Solids*, Academic Press Inc., Orlando, Fla.

Parungo, F., et al. (1997), Asian dust storms and their effects on radiation and climate: part 4, in *Science and Technology Corporation Tech. Rep. 3134*, NOAA, Hampton, Va.

Peterson, J. T. (1968), Measurements of atmospheric aerosols and infrared radiation over northwest India and their interrelationship, Ph.D. thesis, 165 pp., Dep. of Meteorol., Univ. of Wisconsin, Madison, Wis.

Peterson, J. T., and J. A. Weinman (1969), Optical properties of quartz dust particles in infrared wavelengths, *J. Geophys. Res.*, *28*, 6947–6952.

Pollack, J. B., and J. N. Cuzzi (1980), Scattering by nonspherical particles of size comparable with wavelength: A new semi-empirical theory and its application to tropospheric aerosols, *J. Atmos. Sci.*, *37*, 868–881.

Popova, S. I., T. S. Tolstykh, and L. S. Ivlev (1973), Optical constants of Fe_2O_3 in the infrared range of the spectrum, *Opt. Spectrosc.*, *35*, 551–552.

Querry, M. R., G. Osborne, K. Lies, R. Lordon, and R. M. Coveney (1978), Complex refractive index of limestone in the visible and infrared, *Appl. Opt.*, *17*, 353–356.

Reid, J. S., et al. (2003a), Comparison of size and morphological measurements of coarse mode dust particles from Africa, *J. Geophys. Res.*, *108*(D19), 8593, doi:10.1029/2002JD002485.

Reid, E., et al. (2003b), Characterization of African dust transported to Puerto Rico by individual particle and size segregated bulk analysis, *J. Geophys. Res.*, *108*(D19), 8591, doi:10.1029/2002JD002935.

Sikka, D. R. (1977), Desert climate and its dynamics, *Curr. Sci.*, *72*, 35–46.

Singh, S., S. Nath, R. Kohli, and R. Singh (2005), Aerosols over Delhi during pre-monsoon months: Characteristics and effects on surface radiation forcing, *Geophys. Res. Lett.*, *32*, L13808, doi:10.1029/2005GL023062.

Sokolik, I. N., and O. B. Toon (1996), Direct radiative forcing by anthropogenic airborne mineral aerosols, *Nature*, *381*, 681–683.

Sokolik, I. N., and O. B. Toon (1999), Incorporation of mineralogical composition into models of the radiative properties of mineral aerosol from UV to IR wavelengths, *J. Geophys. Res.*, *104*, 9423–9444.

Sokolik, I. N., D. M. Winker, G. Bergametti, D. A. Gillette, G. Carmichael, Y. J. Kaufman, L. Gomes, L. Schuetz, and J. E. Penner (2001), Introduction to special section: Outstanding problems in quantifying the radiative impacts of mineral dust, *J. Geophys. Res.*, *106*, 18,015–18,027.

Tanaka, T. Y., and M. Chiba (2006), A numerical study of the contributions of dust source regions to the global dust budget, *Global Planet. Change*, *52*, 88–104.

Tanré, D., et al. (2003), Measurement and modeling of the Saharan dust radiative impact: Overview of the Saharan Dust Experiment (SHADE), *J. Geophys. Res.*, *108*(D18), 8574, doi:10.1029/2002JD003273.

Tegen, I., P. Hollrig, M. Chin, I. Fung, D. Jacob, and J. Penner (1997), Contribution of different aerosol species to the global aerosol extinction optical thickness: Estimates from model results, *J. Geophys. Res.*, *102*, 23,895–23,915.

Volten, H., O. Minoz, E. Rol, J. D. Haan, W. Vassen, and J. Hovenier (2001), Laboratory measurements of scattering matrices of irregular mineral particles, *J. Geophys. Res.*, *106*, 17,375–17,401.

Wang, M., and H. R. Gordon (1994), Estimating aerosol optical properties over the oceans with the multiangle imaging spectroradiometer: Some preliminary results, *Appl. Opt.*, *33*, 4042–4057.

Weaver, C., P. Ginoux, N. C. Hsu, M. D. Chou, and J. Joiner (2002), Radiative forcing of Saharan dust: GOCART model simulations compared with ERBE data, *J. Atmos. Sci.*, *59*, 736–747.

West, R. L., L. Doose, A. Elbl, M. Tomasko, and M. I. Mishchenko (1997), Laboratory measurements of mineral dust scattering phase function and linear polarization, *J. Geophys. Res.*, *102*, 16,831–16,847.

Yang, P., et al. (2007), Modeling of the scattering and radiative properties of nonspherical dust-like aerosols, *J. Aerosol Sci.*, *38*, 995–1014, doi:10.1016/j.jaerosci.2007.07.001.

―――――――――――――

S. K. Mishra and S. N. Tripathi, Department of Civil Engineering, Indian Institute of Technology Kanpur, Kanpur 208016, India. (snt@iitk.ac.in)